GEOLOGY

Evidence for the charge disproportionation of iron in extraterrestrial bridgmanite

Luca Bindi[1]*, Sang-Heon Shim[2], Thomas G. Sharp[2], Xiande Xie[3]

Bridgmanite, $MgSiO_3$ with perovskite structure, is considered the most abundant mineral on Earth. On the lower mantle, it contains Fe and Al that strongly influence its behavior. Experimentalists have debated whether iron may exist in a mixed valence state, coexistence of Fe^{2+} and Fe^{3+} in bridgmanite, through charge disproportionation. Here, we report the discovery of Fe-rich aluminous bridgmanite coexisting with metallic iron in a shock vein of the Suizhou meteorite. This is the first direct evidence in nature of the Fe disproportionation reaction, which so far has only been observed in some high-pressure experiments. Furthermore, our discovery supports the idea that the disproportionation reaction would have played a key role in redox processes and the evolution of Earth.

INTRODUCTION

High-pressure experiments on lower-mantle compositions suggest that the mineralogy of the lower mantle is dominated by bridgmanite (*1*) with smaller fractions of Fe-bearing periclase and $CaSiO_3$ perovskite (*2*). However, unlike the shallower regions of the mantle, it has been difficult to obtain direct sample representatives of the lower mantle. Although some diamond inclusions have lower mantle–like mineralogy (*3*–*5*), the possible existence of bridgmanite has only been inferred from pyroxene relics in diamond inclusions (*6*, *7*). The diamond inclusions are unlikely to be representative of the lower mantle but, instead, may represent redox fronts (*8*).

Shocked meteorites, extraterrestrial rocks that have experienced high-pressure and high-temperature conditions during collisions in outer space, have provided a suite of natural high-pressure minerals similar to those believed to make up the deep Earth and provide an alternative source of information on deep-mantle mineralogy. These high-pressure minerals occur exclusively in association with shock melt and form either by crystallization of the melts or by solid-state transformation of entrained mineral fragments. Since the discovery of ringwoodite and majorite in shocked chondritic meteorites, many high-pressure minerals have been found in shocked meteorites (*1*, *9*–*12*). Among them, Fe-bearing bridgmanite, $(Mg_{0.75}Fe_{0.25})SiO_3$, in the orthorhombic perovskite structure was recently documented together with Mg-wüstite in shock veins of the Tenham L6 chondrite (*1*, *13*). Bridgmanite is particularly important as it is stable from 660-km depths to near the core-mantle boundary at 2900 km (*14*), thus making up ~38 volume % of our planet.

Here, we report the discovery of the Fe-rich analog of bridgmanite with a composition of $(Fe_{0.54}Mg_{0.37}Al_{0.15}Na_{0.03}Ca_{0.02}Si_{0.89})O_3$ coexisting with metallic iron in a shock vein of the Suizhou meteorite. The discovery represents the first direct evidence in nature of the Fe disproportionation reaction, which so far has only been observed in some high-pressure experiments. Furthermore, this Fe-rich bridgmanite was approved by the International Mineralogical Association (specimen IMA 2019-019) with the name hiroseite in honor of K. Hirose for his fundamental contributions to the discovery of the postperovskite phase in particular and to the mineralogy of mantle perovskite in general (*15*).

[1]Dipartimento di Scienze della Terra, Università degli Studi di Firenze, Via La Pira 4, I-50121 Firenze, Italy. [2]School of Earth and Space Exploration, Arizona State University, Tempe, AZ 85287, USA. [3]Key Laboratory of Mineralogy and Metallogeny/Guangdong Provincial Key Laboratory of Mineral Physics and Materials, Guangzhou Institute of Geochemistry, Chinese Academy of Sciences, Guangzhou 510640, China.
*Corresponding author. Email: luca.bindi@unifi.it

RESULTS

Occurrence of hiroseite

The new mineral was found in the Suizhou meteorite, a heavily shocked (S6) L6 chondrite that contains abundant high-pressure minerals (*16*). In addition to multiple shock veins, Suizhou has local alteration veins that contain Fe-rich silicates such as fayalite. Hiroseite was detected in an Fe-rich grain in shock melt, associated with Fe-bearing periclase $[(Mg_{0.56}Fe_{0.44})O]$, forsteritic olivine $[(Mg_{1.79}Fe_{0.19})Si_{1.01}O_4]$, ringwoodite-ahrensite solid solution $[(Mg_{0.85-1.56}Fe_{0.40-0.91}Al_{0.06-0.07}Ca_{0.06}Na_{0.05})Si_{0.92-1.02}O_4]$, pyroxene $[(Mg_{0.38-0.75}Fe_{0.20-0.40}Na_{0.00-0.08}Al_{0.00-0.04}Ca_{0.01-0.02}Mn_{0.01-0.02})SiO_3]$, $MgSiO_3$ glass $[Mg_{0.99}Fe_{0.04}Ca_{0.02}Mn_{0.01}Si_{0.97}O_3]$, taenite $[Fe_{0.77}Ni_{0.23}]$, and troilite $[Fe_{1.02}S_{0.98}]$ (Fig. 1, A and B, and table S1). The core of this grain consists of hiroseite crystals in a matrix of Fe-bearing periclase, mantled by a rim of ringwoodite-ahrensite solid solution. This assemblage occurs in a small pocket of $MgSiO_3$-rich material that is inferred to be quenched shock melt.

Orthorhombic perovskite structure

The x-ray diffraction pattern (Fig. 1C and fig. S1), obtained using a fragment of hiroseite (approximately 7 μm by 8 μm by 5 μm; see the inset in Fig. 1C) handpicked from the section in Fig. 1B, showed that hiroseite has the orthorhombic perovskite structure with unit-cell parameters of $a = 5.0016(5)$ Å, $b = 7.0031(3)$ Å, $c = 4.8460(3)$ Å, and $V = 169.74(2)$ Å^3. Our Rietveld refinement of the powder diffraction pattern provides an excellent fit ($R_{wp} = 6.83\%$) to the orthorhombic perovskite structure. The observed unit-cell volume is larger than that reported for $MgSiO_3$ bridgmanite (*17*), 162.5 Å^3, consistent with the Fe-rich composition found in our electron microprobe measurements. The A-site occupancy from our refinements is $[Fe_{0.55(2)}Mg_{0.45}]$, which also agrees with our microprobe data (table S1). Taking into account both the microprobe and x-ray diffraction data, the chemical formula of hiroseite can be written as $(Fe^{2+}_{0.44}Mg_{0.37}Fe^{3+}_{0.10}Al_{0.04}Ca_{0.03}Na_{0.02})_{\Sigma1}(Si_{0.89}Al_{0.11})_{\Sigma1}O_3$.

The Raman spectrum of hiroseite (Fig. 1D) is very similar to that reported for synthetic $MgSiO_3$ perovskite (*18*), confirming that hiroseite retains the orthorhombic perovskite structure despite the high concentration of Fe. Phonon mode frequencies are systematically

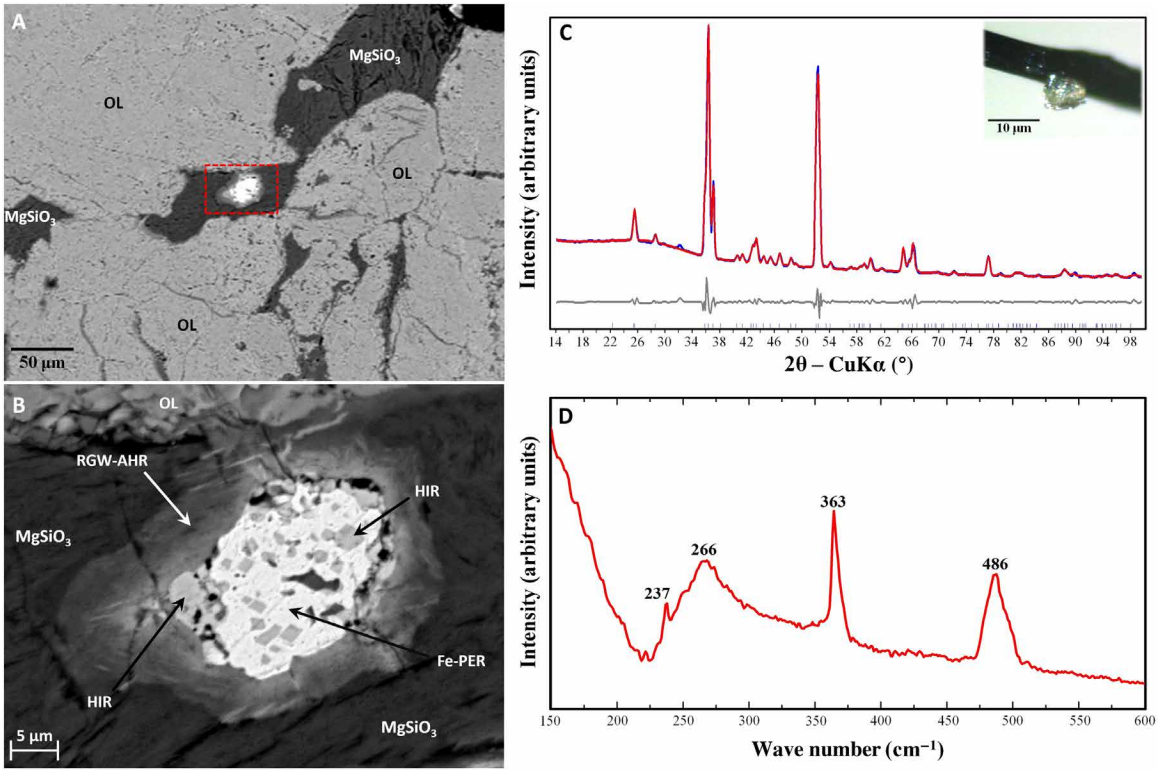

Fig. 1. Fe-rich bridgmanite with the orthorhombic perovskite structure. (**A**) Back-scattered electron–scanning electron microscopy panoramic image of the section containing hiroseite; the abundant light gray material is olivine (OL). (**B**) Enlargement of the red dashed area depicted in (A); hiroseite (HIR) is associated with Fe-bearing periclase (Fe-PER), olivine, ringwoodite-ahrensite (RGW-AHR), and $MgSiO_3$ glass. (**C**) X-ray powder pattern obtained from a hiroseite fragment (in the inset) handpicked from the Suizhou shock vein, shown in the scanning electron microscopy–back-scattered electron images in (B); blue, calculated pattern; red, measured pattern; gray, residual after fitting the powder pattern to account for hiroseite. Tick marks indicate the positions of allowed reflections. Note the presence of a peak ($2\theta \sim 32°$) that does not belong to the hiroseite structure and could be tentatively attributed to very minor siderite, $FeCO_3$. The wavelength of the x-ray beam was 1.54138 Å. (**D**) Raman spectrum for hiroseite.

shifted to lower values, consistent with the analyzed Fe-rich composition. To our knowledge, this spectrum is the first ever reported for a natural $(Mg,Fe)SiO_3$ perovskite.

Charge disproportionation reaction in hiroseite

Because Al-bearing perovskites commonly have high Fe^{3+} contents, it was crucial to investigate the Fe^{2+}/Fe^{3+} ratio in hiroseite. A number of studies indicate that increasing pressure and trivalent cation concentration favor a coupled substitution mechanism, making $FeAlO_3$ and $AlAlO_3$ the most important trivalent perovskite components throughout the lower mantle (*19*, *20*). Elevated concentrations of Fe^{3+} were documented in earlier high-pressure experiments using the multi-anvil press (*21*, *22*). However, because these experiments were performed under relatively oxidizing conditions, it was unclear whether such a large amount of Fe^{3+} could be possible under the more reducing conditions of the lower mantle. In multi-anvil experiments under reducing conditions, Fe^{3+}-rich compositions of aluminous bridgmanite were also found (*23*). It was hypothesized (*23*) that the Fe^{3+} was stabilized through redistribution of electrons in Fe^{2+} to trivalent Fe^{3+} and metallic iron (Fe^0). The study also reported separate metallic iron in their samples to balance the Fe^{3+} in bridgmanite. Although a few similar observations have been documented in high-pressure diamond-anvil cell experiments (*24*), the stability of the reaction remains unclear at the pressures expected for the deep mantle. For example, if a strong thermal gradient exists, then laser heating can produce metallic iron through diffusion (*25*).

Despite the aforementioned uncertainties, the possible charge disproportionation reaction in bridgmanite has been linked to redox reactions in the lower mantle, and its possible impacts on the redox state of shallower regions have been discussed (i.e., the upper mantle and the surface) in a number of models (*23*, *26*–*28*). In principle, the charge disproportionation itself does not change the total number of the nominal charge of Fe ($3Fe^{2+} = 2Fe^{3+} + Fe^0$). However, the most important aspect for the global applications has been the formation of metallic iron. Some models (*23*, *26*) assumed that the greater density of the metallic iron grains from the charge disproportionation would have resulted in the segregation of the metallic iron to the core. However, this segregation would be controlled by the grain boundary properties and the size of the metallic iron grains, which are uncertain in the conditions of the lower mantle (*29*). It is feasible that the higher temperature of the early crystalline mantle might have been more favorable for such a segregation because metallic iron in the warm mantle should have been in the liquid state. The loss of metallic iron to the core would lead to an imbalance between Fe^0 and Fe^{3+} in the lower mantle, effectively increasing its oxidation potential. Once extensive mantle mixing between the upper and the lower mantle started, the excess Fe^{3+} of the lower-mantle materials transported to the upper mantle would have oxidized the region. This idea appears to explain the higher oxygen fugacity found for the upper mantle (*30*). The existence of metallic iron may also affect redox reactions in the contemporary lower mantle. For example, carbon delivered to the lower mantle through subducting

slabs could react with metallic iron from the charge disproportionation reaction, to form iron carbide alloy in the region (*31*). Such a buffering effect of metallic iron in the lower mantle may also affect the speciation of hydrogen (*23*, *32*). The potential importance of the charge disproportionation reaction and its profound implications for redox evolution of the deep mantle and geochemical cycles of important volatiles demand robust constraints on the possible disproportionation reaction in natural systems.

Valence state of iron in hiroseite

An elevated value of $Fe^{3+}/(Fe^{3+} + Fe^{2+})$ (~0.19) is required to charge-balance the chemical composition of hiroseite measured by an electron microprobe (table S1). With some of the Al compensating for the deficiency of Si at the tetrahedral B site, and the remaining Al, as well as Na and Ca, along with Mg and Fe^{2+}, filling the larger A site, charge balance requires 0.10 Fe^{3+} per formula unit (pfu). To measure the finer-scale structure of hiroseite and the Fe^{2+}/Fe^{3+} ratio, we studied a portion of the hiroseite fragment used for the x-ray and Raman investigations by transmission electron microscopy (TEM) coupled with electron energy-loss spectroscopy (EELS). Our TEM measurements showed the presence of isolated nanoscale spheres of metallic iron (Fig. 2 and fig. S2), with a composition of $Fe_{97(3)}Si_{4(1)}$, inside hiroseite. During shock melting, Fe-rich nanoparticles, derived from FeS and FeNi in the host rock, could have been entrapped into silicates crystallizing from shock melt (*33*). However, the absence of S and Ni in the metallic-iron nanoparticles (fig. S3) led us to exclude that hiroseite crystallized from shock-induced melt. Instead, our hiroseite sample formed by a subsolidus transformation. Furthermore, the lack of Mg in our TEM–energy-dispersive spectrometer (EDS) spectra (fig. S3) of the nanoscale particles indicates that the presence of silicon in the metal is an alloy component for metallic iron and not a result of contamination from the surrounding hiroseite.

As there is no evidence of trivalent Fe in the other minerals associated with hiroseite (table S1), we can assume that all the Fe^{3+} in hiroseite, i.e., 0.10 pfu, comes from the disproportionation reaction. According to the charge disproportionation reaction, $3Fe^{2+} = 2Fe^{3+} + Fe^{0}$, the 0.10 Fe^{3+} pfu formed should be accompanied by 0.05 Fe^{0} pfu. If we now calculate the proportion of iron metal with respect to the total iron present in formula units, then it is 0.05/(0.05 + 0.44 + 0.10), which means that about 8.5% of the total Fe should be metal. Hiroseite contains about 34 weight % (wt %) total iron oxide, which includes the metallic Fe nanoparticles in the mineral (table S1); if we take 8.5% of the value, then we obtain 2.9 wt % FeO, which corresponds to 2.3 wt % Fe metal. By a normalization to 100, the 31.1 wt % FeO and 2.3 wt % Fe metal become 93.1 FeO and 6.9 Fe. Taking into account the densities of hiroseite and pure iron (i.e., 5.16 and 7.81 g/cm^3, respectively), we get 96 and 4 volume % of the two components, respectively. We evaluate through image analysis that the amount of metallic iron in hiroseite is 2.6(2) volume %, which is in good agreement with the estimation.

Using the EELS analysis methods of van Aken and Liebscher (*34*), we obtained an Fe^{3+}/Fe_{tot} = 0.12(5) from the EELS spectra of hiroseite (Fig. 3), which compares favorably with that estimated from electron microprobe analyses (i.e., ~0.19). Neglecting the complexity induced by the presence of minor amounts of sodium in hiroseite, the amount of Fe^{3+} (0.10 atoms pfu) is close to but slightly lower than the overall Al content (0.15 atoms pfu), in agreement with the Fe^{3+}/Al ratios found in high-pressure experiments (*23*, *28*, *32*).

DISCUSSION

The bulk shock pressure in the Suizhou meteorite has been estimated to be from 18 to 20 GPa (*16*), but local pressure spikes may have been substantially higher in the first tens of nanoseconds before pressure equilibration was reached. It has been shown that the solubility of Fe in $MgSiO_3$ perovskite increases with pressure (*35*). Hiroseite shows the highest Fe content ever reported among low-Al $MgSiO_3$ perovskite samples. Notwithstanding, such a high Fe content in hiroseite could indicate a shock pressure higher than that previously estimated for the Suizhou meteorite or, alternatively, hiroseite formed metastably from fayalite. Similarly, the temperature of the sample varied greatly, with shock-melt veins and pockets corresponding to the hottest portions of the sample. The $MgSiO_3$-rich shock-melt vein that contains the hiroseite reached temperatures in excess of its liquidus at high pressure (>2000°C), while the entrained Fe-rich olivine fragment that transformed to hiroseite would have reached somewhat lower temperatures. However, fractures or porosity in the olivine fragment could have resulted in higher shock temperatures and localized melting. The presence of aluminum in hiroseite may have

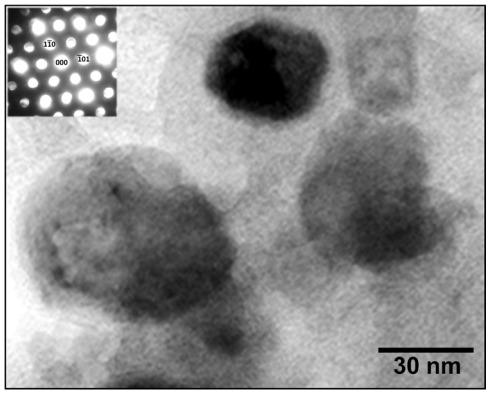

Fig. 2. TEM image of ferric iron–rich hiroseite with nanometric inclusions of metal Fe. The spherically shaped nanoparticles (black in the large image) are metallic iron. Selected area diffraction pattern down [111] for one of the metallic Fe spheres is shown in the inset. The amount of metallic Fe in hiroseite is estimated to be 2.6(2) volume % through image analysis.

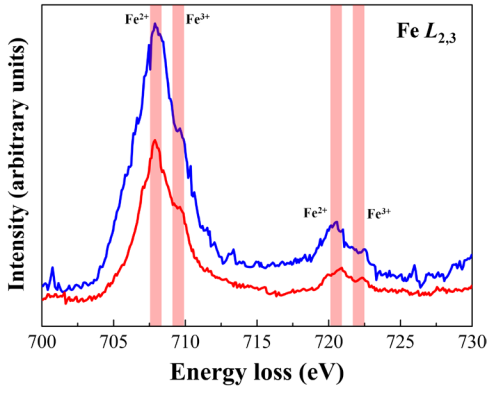

Fig. 3. Measuring the $Fe^{3+}/(Fe^{2+} + Fe^{3+})$ ratio in hiroseite. Two electron energy-loss spectra (red and blue) in the region 700 to 730 eV obtained at different spots in the hiroseite sample.

been incorporated from the surrounding $MgSiO_3$-rich shock melt or from inclusions within the olivine. Al diffusion from either source is likely to be fast enough at $T > 2000$°C.

The textures and compositions of the hiroseite-bearing grain suggest the transformation of a chemically zoned olivine. The fayalite-rich core transformed to hiroseite plus Fe-bearing periclase, while the less fayalite-rich rim transformed to a ringwoodite-ahrensite solid solution. The mechanism of hiroseite formation thus appears to be a subsolidus disproportionation reaction (eutectoid reaction) of fayalite to hiroseite plus Fe-bearing periclase. Although this reaction occurred at substantially higher temperatures than that of the present-day mantle geotherm, the temperature is more relevant for that of the mantle expected for the early Earth where an "oxygen pump" might have been important in increasing the oxygen fugacity of the upper mantle (*26*). Last, our discovery demonstrates that the disproportionation of Fe^{2+} to Fe^0 and Fe^{3+} does occur in a natural high-pressure environment and therefore is likely to occur in Earth's mantle as well.

MATERIALS AND METHODS

Scanning electron microscopy

The instrument used was a ZEISS EVO MA15 scanning electron microscope coupled with an Oxford INCA 250 EDS, operating at 25-kV accelerating potential, 500-pA probe current, 2500 counts/s as the average count rate on the whole spectrum, and a counting time of 500 s. The sample was sputter-coated with 30-nm-thick carbon film.

Electron microprobe

Major and minor elements were determined using a JEOL JXA-8200 electron microprobe operating at 15-kV accelerating voltage and 40-nA beam current (and a 1-μm beam diameter), with variable counting times: 30 s was used for Mg, Fe, and Si, and 100 s was used for the minor elements Al, Ca, and Na. Matrix correction was performed using the Bence and Albee program (*36*) modified by Albee and Ray (*37*). Replicate analyses of augite USNM 122142 were used to check accuracy and precision. The standards used were plagioclase (Ca), forsterite (Mg, Si), fayalite (Fe), and albite (Na, Al).

Transmission electron microscopy

Measurements were conducted using a Jeol JEM 2010, an accelerating voltage of 200 kV, an ultrahigh-resolution pole piece, and a point-to-point resolution close to 1.9 Å (the electron probe can be focused down to 100 Å in diameter). The microscope is equipped with a semi–scanning transmission electron microscopy system and an EDS (ISIS Oxford, superthin window). A small amount (about 1.5 to 2.0 μm) of the grain shown in the inset of Fig. 1C (the same specimen used for the x-ray diffraction and Raman spectroscopy study) was placed on a Cu mesh grid (300 mesh, 3 mm in diameter) that had been previously covered by a thin carbon layer (support film). The powdered grid was further coated by carbon. Selected area diffraction patterns were collected on the Fe nanoparticles encased in bridgmanite. In particular, we collected a good electron diffraction pattern corresponding to the [111] zone axis of *bcc* iron. Measured interplanar distances are as follows: d_{-101} = 2.023(5) Å and d_{1-10} = 2.024(4) Å. TEM-EDS analyses collected on the nanoparticles (fig. S3) gave the following mean values (in weight % of elements and with the SDs in parentheses): Fe 96.5(2.7) and Si 3.5(1.2).

Raman spectroscopy

A Raman spectrum was obtained using a micro/macro Jobin Yvon LabRAM HRVIS, equipped with a motorized *x*-*y* stage and an Olympus microscope. The backscattered Raman signal was collected with 50× objective, and the Raman spectrum was obtained for a randomly oriented crystal. The 632.8-nm line of a He-Ne laser was used as excitation; laser power on the sample (2 mW) was controlled by a series of density filters. The lateral and depth resolutions were about 2 and 5 μm, respectively. The system was calibrated using the 520.6 cm^{-1} Raman band of silicon before the experimental session. Spectra were collected with multiple acquisitions (two to six) with single counting times ranging between 20 and 180 s. The spectra were recorded using the LabSpec 5 program from 150 to 1300 cm^{-1}. Since no peaks were discernible in the range of 600 to 1300 cm^{-1}, we presented spectra from 150 to 600 cm^{-1}.

Following Williams *et al.* (*18*), we assigned the Raman peak at 486 cm^{-1} to an A_g mode derived from the breathing vibration (A_{1g}) of the octahedral SiO_6 group. The strongest peak at 363 cm^{-1} can be assigned to the E_g type of motion. The lowest (and broadest) frequency modes in the Raman spectrum, at 266 and 237 cm^{-1}, were probably due to complex vibrations derived from octahedral deformations and rotational motions coupled to displacements of the dodecahedral cations. All the observed Raman peaks were displaced toward higher frequencies with respect to pure $MgSiO_3$ (*18*).

Electron energy loss spectroscopy

EELS spectra were collected with the TEM described above using a beam size, at the sample, of 25 nm and an accelerating voltage at 140 kV to reduce the electron beam damage of the sample. The measurement was performed with a Gatan Continuum spectrometer with an energy resolution of 0.7 to 0.8 eV. Using the EELS analysis methods given by van Aken and Liebscher (*34*), we obtained an Fe^{3+}/Fe_{tot} = 0.12(5), which compares favorably with that estimated from electron microprobe analyses (~0.19).

X-ray diffraction

A small hiroseite fragment (size about 7 μm by 8 μm by 5 μm) was extracted from the polished section under a reflected light microscope from the region in Fig. 1B and mounted on a 5-μm-diameter carbon fiber, which was, in turn, attached to a glass rod (see inset of Fig. 1C).

Single-crystal x-ray diffraction

Single-crystal x-ray studies were carried out using a Bruker D8 Venture equipped with a Photon III charge-coupled device (CCD) detector, with graphite-monochromatized MoKα radiation (λ = 0.71073 Å), under working conditions of 60-kV accelerating voltage and 300-s exposure time per frame; the detector-to-sample distance was 6 cm. The sample turned out to be polycrystalline with broad single-crystal diffraction effects (fig. S1).

X-ray powder diffraction

X-ray powder diffraction data (table S2) were obtained with Bruker D8 Venture equipped with a Photon III CCD detector, with graphite-monochromatized CuKα radiation (λ = 1.54138 Å) and with 4 hours of exposure; the detector-to-sample distance was 7 cm. The program APEX3 was used to convert the measured diffraction rings to a conventional powder diffraction pattern, which was indexed on the basis of the Al-bearing $MgSiO_3$ perovskite structure (*38*). A very weak peak (i.e., d = 2.79 Å) did not belong to the perovskite structure and could be tentatively attributed to very minor siderite,

$FeCO_3$. The least-squares refinement, based on the Pawley method (R_{wp} = 3.80%), gave the following values: a = 5.0016(5) Å, b = 7.0031(3) Å, c = 4.8460(3) Å, V = 169.74(2) Å^3, Z = 4, and space group *Pnma*.

The absence of diffraction peaks belonging to iron (known to be present by the TEM study in a proportion close to ~4 volume %) is expected as the three diffraction peaks of *bcc* Fe in the 2θ range investigated are hidden by the perovskite peaks. Furthermore, the strongest peak of iron at 2θ = 44.72° (d = 2.027 Å) should show a calculated intensity (assuming that its diffraction quality is almost the same as that of hiroseite), which clearly goes slightly above the background.

Rietveld crystal-structure refinement

The crystal structure of hiroseite was refined with the program TOPAS (*39*) starting from the atomic coordinates reported for the Al-bearing $MgSiO_3$ perovskite structure (*38*) with initial values for isotropic temperature factors (U_{iso}) arbitrarily chosen as 0.04 Å^2 for the A site, 0.02 Å^2 for the B site, and 0.025 Å^2 for O. A shifted Chebyshev with six coefficients and a pseudo-Voigt function were used to fit background and peak shape, respectively. Cell parameters, scale factor, and the background polynomial functions were free variables during refinement. Absorption correction was not performed, given the very low microroentgen value (i.e., ~0.5) of hiroseite. Parameters were added to the refinement in the following order: peak shape, peak asymmetry, atomic coordinates, and isotropic temperature factors. Although we only have powder data collected on a fragment <10 μm across, the refinement converged smoothly (R_{wp} = 6.83%, R_{exp} = 5.85%, R_p = 4.58%, and χ^2 = 1.36; R_{Bragg} = 3.60% using 125 observed reflections), and we were also able to refine the atom coordinates and the site occupancy at the A site (using Mg^{2+} versus Fe^{2+} as scattering curves). The refinement of the site occupancy at the A site gave the $[Fe_{0.55(2)}Mg_{0.45}]$ population, in excellent agreement with the electron microprobe data. Although some of the intensities do not match perfectly those that one can calculate taking into account the site occupancies and the atom coordinates of hiroseite (tables S1 and S3), we think that the quality of the data (obtained from a fragment <10 μm across) is sufficiently robust to prove the entry of Fe into the structure. Furthermore, the unit-cell parameters were also influenced by the entry of Fe into the structure. We observed a general increase in all the values of about 1% with respect to pure $MgSiO_3$ (*17*) and an overall increase in the unit-cell volume, which passes from 162.5 Å^3 in pure $MgSiO_3$ (*17*) to 169.74 Å^3 in hiroseite (fig. S4). We hypothesized that both Fe^{2+} and Fe^{3+} replace Mg at the dodecahedral site (A), whereas minor Al enters the octahedral site (B) with the available Si.

The mean bond distance at the A site (2.28 Å) is greater than that in pure $MgSiO_3$ (2.21 Å) (*17*). Note that the ionic radius of Mg in eightfold coordination is 0.89 Å (*40*). Thus, the ratio between 0.89 and 2.21 (i.e., ⟨A-O⟩ in bridgmanite) is equal to 0.403. If we consider the A-site population in hiroseite from electron microprobe data, i.e., $(Fe^{2+}_{0.44}Mg_{0.37}Fe^{3+}_{0.10}Al_{0.04}Ca_{0.03}Na_{0.02})\Sigma_1$, and the ionic radii in eightfold coordination of these elements from Shannon (*40*), we obtain an average radius of 0.92 Å. If we use the value of 0.403 as the starting point [as the pure $MgSiO_3$ structure has been refined by x-ray single-crystal data (*17*)], we can write 0.92/0.403 = 2.28 Å, which is exactly the ⟨A-O⟩ value we observe from the structure refinement. This provides additional evidence for the estimated Fe^{2+}/Fe^{3+} based on charge balance of chemical data. Atomic coordinates are given in table S3. Bond distances are given in table S4. The list of observed and calculated structure factors and the Crystallographic Information File (CIF) (CCDC 1936917) can be obtained free of charge from the Cambridge Crystallographic Data Centre via www.ccdc.cam.ac.uk/data_request/cif.

SUPPLEMENTARY MATERIALS

Supplementary material for this article is available at http://advances.sciencemag.org/cgi/content/full/6/2/eaay7893/DC1

Fig. S1. Experimental x-ray diffraction image of hiroseite.
Fig. S2. TEM image of hiroseite.
Fig. S3. TEM-EDS spectra collected on the Fe nanofragments embedded in hiroseite.
Fig. S4. Bridgmanite-hiroseite series.
Table S1. Electron microprobe analyses of minerals of the Suizhou meteorite.
Table S2. X-ray powder diffraction data (*d* in angstroms) for hiroseite.
Table S3. Atoms, site occupancy factors (s.o.f.), fractional coordinates of atoms, and B_{eq} in the structure of hiroseite.
Table S4. Selected bond distances (in angstroms) in the structure of hiroseite.
References (*41*–*45*)

REFERENCES AND NOTES

1. O. Tschauner, C. Ma, J. R. Beckett, C. Prescher, V. B. Prakapenka, G. R. Rossman, Discovery of bridgmanite, the most abundant mineral in Earth, in a shocked meteorite. *Science* **346**, 1100–1102 (2014).
2. F. Nestola, N. Korolev, M. Kopylova, N. Rotiroti, D. G. Pearson, M. G. Pamato, M. Alvaro, L. Peruzzo, J. J. Gurney, A. E. Moore, J. Davidson, $CaSiO_3$ perovskite in diamond indicates the recycling of oceanic crust into the lower mantle. *Nature* **555**, 237–241 (2018).
3. B. Harte, J. W. Harris, M. T. Hutchinson, G. R. Watt, M. C. Wilding, Lower mantle mineral associations in diamonds from Sao Luiz, Brazil. *Geochem. Soc. Spec. Publ.* **6**, 125–153 (1999).
4. T. Stachel, G. P. Brey, J. W. Harris, Inclusions in sublithospheric diamonds: Glimpses of deep Earth. *Elements* **1**, 73–78 (2005).
5. F. V. Kaminsky, Mineralogy of the lower mantle: A review of "super-deep" mineral inclusions in diamond. *Earth Sci. Rev.* **110**, 127–147 (2012).
6. S. E. Kesson, J. D. Fitz Gerald, Partitioning of MgO, FeO, NiO, MnO and Cr_2O_3 between magnesian silicate perovskite and magnesiowüstite: Implications for the origin of inclusions in diamond and the composition of the lower mantle. *Earth Planet. Sci. Lett.* **111**, 229–240 (1992).
7. F. E. Brenker, T. Stachel, J. W. Harris, Exhumation of lower mantle inclusions in diamond; a TEM investigation of retrograde phase transitions, reactions and exsolution. *Earth Planet. Sci. Lett.* **198**, 1–9 (2002).
8. M. J. Walter, S. C. Kohn, D. Araujo, G. P. Bulanova, C. B. Smith, E. Gaillou, J. Wang, A. Steele, S. B. Shirey, Deep mantle cycling of oceanic crust: Evidence from diamonds and their mineral inclusions. *Science* **334**, 54–57 (2011).
9. R. D. Price, A. Putnis, S. O. Agrell, D. G. W. Smith, Wadsleyite, natural beta-$(Mg,Fe)_2SiO_4$ from the Peace River meteorite. *Can. Mineral.* **21**, 29–35 (1983).
10. N. Tomioka, K. Fujino, Natural $(Mg,Fe)SiO_3$-ilmenite and -perovskite in the Tenham meteorite. *Science* **277**, 1084–1086 (1997).
11. T. G. Sharp, C. M. Lingemann, C. Dupas, D. Stöffler, Natural occurrence of $MgSiO_3$-ilmenite and evidence for $MgSiO_3$-perovskite in a shocked L chondrite. *Science* **277**, 352–355 (1997).
12. L. Bindi, M. Chen, X. Xie, Discovery of the Fe-analogue of akimotoite in the shocked Suizhou L6 chondrite. *Sci. Rep.* **7**, 42674 (2017).
13. C. Ma, O. Tschauner, J. R. Beckett, Y. Liu, G. R. Rossman, S. V. Sinogeikin, J. S. Smith, L. A. Taylor, Ahrensite, γ-Fe_2SiO_4, a new shock-metamorphic mineral from the Tissint meteorite: Implications for the Tissint shock event on Mars. *Geochim. Cosmochim. Acta* **184**, 240–256 (2016).
14. M. Murakami, K. Hirose, N. Sata, Y. Ohishi, Post-perovskite phase transition and mineral chemistry in the pyrolytic lowermost mantle. *Geophys. Res. Lett.* **32**, L03304 (2005).
15. K. Hirose, R. Sinmyo, J. Hernlund, Perovskite in Earth's deep interior. *Science* **358**, 734–738 (2017).
16. X. Xie, M. Chen, Shock-induced redistribution of trace elements, in *Suizhou Meteorite: Mineralogy and Shock Metamorphism* (Springer, 2016), pp. 211–223.
17. D. P. Dobson, S. D. Jacobsen, The flux growth of magnesium silicate perovskite single crystals. *Am. Mineral.* **89**, 807–811 (2004).
18. Q. Williams, R. Jeanloz, P. McMillan, Vibrational spectrum of $MgSiO_3$ perovskite: Zero-pressure Raman and mid-infrared spectra to 27 GPa. *J. Geophys. Res.* **92**, 8116–8128 (1987).
19. M. J. Walter, R. G. Trønnes, L. S. Armstrong, O. T. Lord, W. A. Caldwell, S. M. Clark, Subsolidus phase relations and perovskite compressibility in the system MgO–$AlO_{1.5}$–SiO_2 with implications for Earth's lower mantle. *Earth Planet. Sci. Lett.* **248**, 77–89 (2006).

20. F. Zhang, A. R. Oganov, Valence state and spin transitions of iron in Earth's mantle silicates. *Earth Planet. Sci. Lett.* **249**, 436–443 (2006).
21. C. A. McCammon, Perovskite as a possible sink for ferric iron in the lower mantle. *Nature* **387**, 694–696 (1997).
22. S. Lauterbach, C. A. McCammon, P. van Aken, F. Langenhorst, F. Seifert, Mössbauer and ELNES spectroscopy of (Mg,Fe)(Si,Al)O_3 perovskite: A highly oxidized component of the lower mantle. *Contrib. Mineral. Petrol.* **138**, 17–26 (2000).
23. D. J. Frost, C. Liebske, F. Langenhorst, C. A. McCammon, R. G. Trønnes, D. C. Rubie, Experimental evidence for the existence of iron-rich metal in the Earth's lower mantle. *Nature* **248**, 409–412 (2004).
24. R. Sinmyo, C. A. McCammon, L. Dubrovinsky, The spin state of Fe^{3+} in lower mantle bridgmanite. *Am. Mineral.* **102**, 1263–1269 (2017).
25. M. Fialin, G. Catillon, D. Andrault, Disproportionation of Fe^{2+} in Al-free silicate perovskite in the laser heated diamond anvil cell as recorded by electron probe microanalysis of oxygen. *Phys. Chem. Miner.* **36**, 183–191 (2009).
26. B. J. Wood, Phase transformations and partitioning relations in peridotite under lower mantle conditions. *Earth Planet. Sci. Lett.* **174**, 341–354 (2000).
27. D. Andrault, M. Muñoz, G. Pesce, V. Cerantola, A. Chumakov, I. Kantor, S. Pascarelli, R. Rüffer, L. Hennet, Large oxygen excess in the primitive mantle could be the source of the Great Oxygenation Event. *Geochem. Perspect. Lett.* **6**, 5–10 (2018).
28. S.-H. Shim, B. Grocholski, Y. Ye, E. E. Alp, S. Xu, D. Morgan, Y. Meng, V. B. Prakapenka, Stability of ferrous-iron-rich bridgmanite under reducing midmantle conditions. *Proc. Natl. Acad. Sci. U.S.A.* **114**, 6468–6473 (2017).
29. C. Y. Shi, L. Zhang, W. Yang, Y. Liu, J. Wang, Y. Meng, J. C. Andrews, W. L. Mao, Formation of an interconnected network of iron melt at Earth's lower mantle conditions. *Nat. Geosci.* **6**, 971–975 (2013).
30. D. J. Frost, R. Myhill, Chemistry of the lower mantle, in *Deep Earth: Physics and Chemistry of the Lower Mantle and Core, Geophysical Monograph 217*, H. Terasaki, R. A. Fischer, Ed. (American Geophysical Union, John Wiley & Sons Inc., ed. 1, 2016).
31. A. Rohrbach, M. W. Schmidt, Redox freezing and melting in the Earth's deep mantle resulting from carbon-iron redox coupling. *Nature* **472**, 209–212 (2011).
32. D. J. Frost, C. A. McCammon, The redox state of Earth's mantle. *Annu. Rev. Earth Planet. Sci.* **36**, 389–420 (2008).
33. A. Leroux, J.-C. Doukhan, F. Guyot, Metal-silicate interaction in quenched shock-induced melt of the Tenham L6 chondrite. *Earth Planet. Sci. Lett.* **179**, 477–487 (2000).
34. P. A. van Aken, B. Liebscher, Quantification of ferrous/ferric ratios in minerals: New evaluation schemes of Fe L_{23} electron energy-loss near-edge spectra. *Phys. Chem. Miner.* **29**, 188–200 (2002).
35. Y. Tange, E. Takahashi, Y. Nishihara, K.-i. Funakoshi, N. Sata, Phase relations in the system MgO-FeO-SiO_2 to 50 GPa and 2000°C: An application of experimental techniques using multianvil apparatus with sintered diamond anvils. *J. Geophys. Res.* **114**, B02214 (2009).
36. A. E. Bence, A. L. Albee, Empirical correction factors for the electron microanalysis of silicate and oxides. *J. Geol.* **76**, 382–403 (1968).
37. A. L. Albee, L. Ray, Correction factors for electron probe analysis of silicate, oxides, carbonates, phosphates, and sulfates. *Anal. Chem.* **42**, 1408–1414 (1970).
38. H. Kojitani, T. Katsura, M. Akaogi, Aluminum substitution mechanisms in perovskite-type $MgSiO_3$: An investigation by Rietveld analysis. *Phys. Chem. Miner.* **34**, 257–267 (2007).
39. A. A. Coelho, TOPAS and TOPAS-Academic: An optimization program integrating computer algebra and crystallographic objects written in C++. *J. Appl. Crystallogr.* **51**, 210–218 (2018).
40. R. D. Shannon, Revised effective ionic radii and systematic studies of interatomic distances in halides and chalcogenides. *Acta Crystallogr.* **32**, 751–767 (1976).
41. K. Catalli, S.-H. Shim, V. B. Prakapenka, J. Zhao, W. Sturhahn, P. Chow, Y. Xiao, H. Liu, H. Cynn, W. J. Evan, Spin state of ferric iron in $MgSiO_3$ perovskite and its effect on elastic properties. *Earth Planet. Sci. Lett.* **289**, 68–75 (2010).
42. T. B. Ballaran, A. Kurnosov, K. Glazyrin, D. J. Frost, M. Merlini, M. Hanfland, R. Caracas, Effect of chemistry on the compressibility of silicate perovskite in the lower mantle. *Earth Planet. Sci. Lett.* **333–334**, 181–190 (2012).
43. C. B. Vanpeteghem, J. Zhao, R. J. Angel, N. L. Ross, N. Bolfan-Casanova, Crystal structure and equation of state of $MgSiO_3$ perovskite. *Geophys. Res. Lett.* **33**, L03306 (2006).
44. Y. Kudoh, C. T. Prewitt, L. W. Finger, A. Darovskikh, E. Ito, Effect of iron on the crystal-structure of (Mg,Fe)SiO_3 perovskite. *Geophys. Res. Lett.* **17**, 1481–1484 (1990).
45. D. R. Hummer, Y. W. Fei, Synthesis and crystal chemistry of Fe^{3+}-bearing (Mg,Fe^{3+})(Si,Fe^{3+})O_3 perovskite. *Am. Mineral.* **97**, 1915–1921 (2012).

Acknowledgments: We thank W. Griffin, K. Hirose, R. Hemley, F. Nestola, V. Stagno, and N. Tomioka for useful discussions and L. Chelazzi for assistance with x-ray diffraction experiments. **Funding:** L.B. was funded by MIUR-PRIN2017, project "TEOREM—deciphering geological processes using Terrestrial and Extraterrestrial ORE Minerals", prot. 2017AK8C32 (PI: L.B.), and the "60%-2017" research funds from the University of Firenze, Italy. S.-H.S. was supported by NSF (EAR-1725094 and EAR-1338810) and NASA (NExSS). T.G.S. was supported by NASA Emerging Worlds Grant 80NSSC18K0591. **Author contributions:** L.B. found hiroseite, led the proposal of new mineral species to the International Mineralogical Association, and analyzed the Suizhou thin section by scanning electron microscopy, electron probe microanalysis, Raman spectroscopy, and TEM. L.B., S.-H.S., T.G.S., and X.X. discussed the results. L.B., S.-H.S., and T.G.S. wrote the paper. **Competing interests:** The authors declare that they have no competing interests. **Data and materials availability:** All data needed to evaluate the conclusions in the paper are present in the paper and/or the Supplementary Materials. Crystallographic data (CCDC 1936917) can be obtained free of charge from the Cambridge Crystallographic Data Centre via www.ccdc.cam.ac.uk/data_request/cif. Raw Raman, EELS, and all additional data are available from the authors upon request.

Submitted 18 July 2019
Accepted 14 November 2019
Published 10 January 2020
10.1126/sciadv.aay7893

Citation: L. Bindi, S.-H. Shim, T. G. Sharp, X. Xie, Evidence for the charge disproportionation of iron in extraterrestrial bridgmanite. *Sci. Adv.* **6**, eaay7893 (2020).